Journal of Geochemical Exploration 196 (2019) 81–94

Contents lists available at ScienceDirect

Journal of Geochemical Exploration

journal homepage: www.elsevier.com/locate/gexplo

Interpreting element addition and depletion at the Ann Mason porphyry-Cu deposit, Nevada, using mapped mass balance patterns

Ayesha D. Ahmed[a,*], Shawn B. Hood[a], Michael F. Gazley[b], David R. Cooke[a], Evan A. Orovan[a]

[a] University of Tasmania – TMVC (The Mining Value Chain), Hobart, Tasmania 7005, Australia
[b] RSC Mining and Mineral Exploration, 93 The Terrace, Wellington, 6000, New Zealand

A B S T R A C T

Elemental mass changes were calculated for 154 samples from four rock types around the Ann Mason porphyry-Cu-(Mo−Au) deposit, Yerington district, Nevada. The purpose of these calculations was to investigate addition and depletion patterns in two-dimensional (2-D) map space. Mass changes in Ca, Mg, Na, P, Cu, Mo, As, Sb, Sr, and Pb from samples in the pre- to *syn*-mineralisation Yerington batholith vary systematically with lateral and vertical distance from the Ann Mason deposit. At the core of the Ann Mason deposit, Cu and Mo were strongly added (> 10,000% relative to average protolith values), with restricted lateral mass addition halos around the deposit. Copper is depleted in wall rocks surrounding the deposit. Calcium and Sr were removed (up to 98% depletion) from parts of the deposit centre due to the destruction of calcic-plagioclase and other calcium-bearing minerals during potassic alteration. Calcium (up to 1570%) and Sr (up to 315%) were added outside the deposit and were concentrated around 4 km from the deposit centre where epidote alteration is most intense. Arsenic and Sb were removed from the deposit centre (up to 99% depletion) where silicate-mineral alteration assemblages dominate. Antimony shows an addition halo (ranging from 25% up to 1900%) that extends from the deposit centre 500 m laterally away, and correlates spatially with the increased abundance of pyrite that typically surrounds porphyry deposits. Epidote-altered samples of Shamrock monzonite from outside the Casting Copper skarn show addition of Ca (up to 196%), Sb (up to 1100%), and depletion of Na (up to −98%). Samples from the central part of the post-mineralisation Shamrock monzonite record lower mass changes in Mg, Ca, P, and Mo, compared to other parts of the batholith. Some samples from the northern contact of the Shamrock batholith exhibit addition of Ca (up to 554%), Sr (up to 504%), and depletion in Na (up to −98%). These samples are coincident with strong epidote alteration.

Our results provide a rock-normalised geochemical map that reflects quantified element addition and depletion patterns, which is useful for interrogating geological processes at a regional scale. Although interpreting relative element addition and depletion in map space is possible using conventional immobile element ratio approaches, mass balance calculations provide the benefit of quantified results.

1. Introduction

Initial interpretation of ore-forming processes in a mineralised district is often undertaken using spatially represented geochemical concentration data (Reimann, 2005; McKinley et al., 2016; Zuo et al., 2016). Identification of prospective anomalies or geochemical processes involves recognising geochemical patterns related to mineral deposits or associated metasomatism of host rocks (Reimann, 2005; Zuo et al., 2013). While geological knowledge helps to inform what values are considered 'typical', 'background', or 'anomalous', further processing is required to normalise and quantify these data (Aitchison, 1989; Govett, 1983; Grant, 1986; Reimann, 2005; McKinley et al., 2016).

Use of relatively low and high univariate values to represent element depletion and addition, respectively, is problematic when multiple rock types are present in an area. Element values in this case can represent a combination of protolith composition, the effects of alteration or mineralisation, and weathering. Approaches to examining geochemical changes while accounting for protolith composition include: (1) assessing geochemical datasets relative to average crustal abundance for elements of interest (Govett, 1983; Brauhart et al., 2017); (2) ratioing single elements to another element not typically affected by metasomatic processes such as Al, Ti, Y, or Zr (immobile elements; Winchester and Floyd, 1977; Floyd and Winchester, 1978; MacLean and Barrett, 1993; Rollinson, 1993; Brand, 1999); (3) calculating 'enrichment factors' using the proportion between two ratios, one representing a sample and one representing average crustal abundance, where the element concentration of interest is divided by the concentration of an immobile element (Chandrajith et al., 2001; El-Makky and Sediek, 2012; Gong et al., 2013; Yaylalı-Abanuz, 2013; Wang et al., 2013; Liu et al., 2014; Hosseini-Dinani et al., 2015; Chen et al., 2017; Carranza, 2017; Brauhart et al., 2017) and (4) calculating mass balance, where the ratio of immobile element concentration for an altered and unaltered (or least-altered) sample provide a reference frame for computing element addition or loss (Gresens, 1967; Grant, 1986; Grant, 2005). While methods 1 and 2 account for protolith composition, they represent relative values and do not quantify chemical changes. Method

* Corresponding author.
E-mail address: ayesha.ahmed@utas.edu.au (A.D. Ahmed).

https://doi.org/10.1016/j.gexplo.2018.09.009
Received 4 April 2018; Received in revised form 19 July 2018; Accepted 28 September 2018
Available online 12 October 2018
0375-6742/

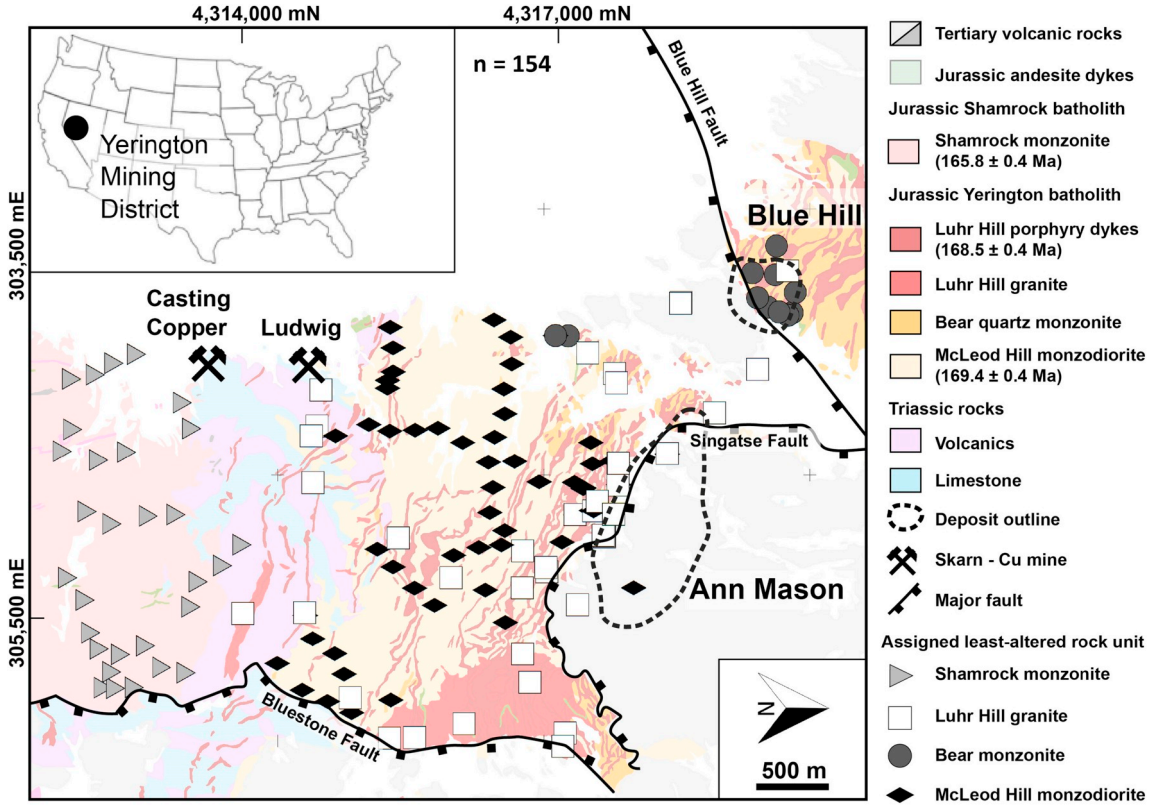

Fig. 1. Geology map of the Ann Mason fault block in the Yerington Mining District, Nevada modified from Proffett Jr. and Dilles (1984). U—Pb zircon ages from Dilles and Wright (1988). The map has been rotated 90° towards the east to show paleo-relationships between lithological units, prior to Basin and Range faulting, which tilted all Mesozoic units nearly 90° to the west (Proffett Jr. and Dilles, 1984; Dilles, 1984, 1987; Richardson and Seedorff, 2015). Stippled outlines indicate the extent of the 2015 Cu resources at the Ann Mason and Blue Hill deposits projected to surface (Watkins et al., 2015). The location of Cu-skarn deposits in the Ann Mason fault block are shown (Casting Copper and Ludwig deposits). Skarn deposits outside the Ann Mason fault block are not shown (Bluestone and Mason Valley Copper). Black symbols mark sample locations. Sample locations and descriptions are included in Appendix A. (For interpretation of the references to colour in this figure legend, the reader is referred to the web version of this article.)

3 does provide a general chemical reference frame for lithological groups but does not consider variation in lithology. Method 4, mass balance, accounts for variations in host rock geology and provides a quantified measure of chemical change. We present and discuss the mapping of mass balance data as an effective way to represent and understand alteration effects at a district scale, with a focus on the Ann Mason porphyry-Cu-(Mo—Au) deposit, Yerington district, Nevada. A modified method to those outlined by Gresens (1967) and Grant (1986, 2005) is used to produce plan maps of quantified concentration changes in Ca, Mg, Na, P, Cu, Mo, Sb, As, Pb, and Sr. The approach quantifies more accurately the relative addition or depletion of elements and facilitates the interpretation of metasomatic and mineralising processes.

2. Geology of the Ann Mason fault block

The Yerington mining district (Yerington) is in western Nevada, United States (Fig. 1). The Yerington district and associated porphyry-Cu-(Mo—Au) and skarn-Cu deposits have been mapped and studied extensively (Fig. 1; Einaudi, 1977; Harris and Einaudi, 1982; Proffett and Dilles, 1984; Dilles, 1987; Battles, 1990; Dilles and Einaudi, 1992; Dilles et al., 1992; Dilles and Proffett, 1995; Dilles et al., 1995; Dilles et al., 2000; Lipske, 2002; Cohen, 2011; Richardson and Seedorff, 2015; Dilles et al., 2015; Schöpa et al., 2017). During the Early Miocene (~17 Ma), large-scale crustal extension resulted in the tilting of major fault blocks 60–90° to the west, exposing vertical cross sections through several porphyry deposits in the district (Proffett Jr., 1977; Proffett Jr. and Dilles, 1984; Richardson and Seedorff, 2015). This exposure allows for systematic mapping of changes in whole-rock chemistry across the top, bottom, and one side (southern side) of the Ann Mason deposit, for rocks originally located up to 6 km below the Earth's surface.

2.1. The Ann Mason deposit

The Ann Mason deposit has a combined measured mineral resource of 412 Mt. at 0.33% Cu, 0.006% Mo, 0.03 g/t Au, and 0.64 g/t Ag (Kulla et al., 2017). Ann Mason, and other porphyry-Cu and skarn-Cu deposits in the district (e.g., Casting Copper, and Ludwig), are associated with the Jurassic Yerington batholith (Fig. 1; Knopf, 1918; Proffett Jr. and Dilles, 1984; Dilles, 1987; Dilles and Wright, 1988), a medium- to high-K, calc-alkaline, polyphase intrusive complex. The batholith intruded a sequence of Triassic to Jurassic sedimentary and volcanic rocks over a period of one million years (Dilles and Wright, 1988). The intrusive phases are the McLeod Hill monzodiorite (Fig. 2A; 169.4 ± 0.4 Ma; Dilles and Wright, 1988), the Bear quartz monzonite (Fig. 2B), and the Luhr Hill granite (Fig. 2C) with its associated granite porphyry dykes (Fig. 2D; 168.5 ± 0.4 Ma; Dilles and Wright, 1988). The Shamrock monzonite (Fig. 2E) intruded the same Triassic to Jurassic volcanic-sedimentary package at 165.8 ± 0.4 Ma and is considered to post-date Cu-mineralisation (Dilles and Wright, 1988). Tertiary volcanic rocks cover much of the northern part of the Yerington district (Fig. 1).

The Ann Mason deposit is localised in and around the Luhr Hill granite porphyry dyke swarm in the Ann Mason fault block (Fig. 1; Proffett and Dilles, 1984; Dilles, 1987). Magmatic-hydrothermal fluids were sourced from the Luhr Hill granite and associated dykes (Dilles, 1987; Dilles and Einaudi, 1992; Dilles et al., 1995). Host rocks to mineralisation include the McLeod Hill monzodiorite, which extends 4 km

south from the deposit centre. The deposit centre is defined here a central zone within the 0.15% Cu grade shell projected to surface (Fig. 1). Further south, Mesozoic volcanic and sedimentary rocks separate the Yerington batholith from the Shamrock batholith (Fig. 1). At Ann Mason, Cu, Mo, and Au grades are directly correlated with vein density (Dilles and Einaudi, 1992; Dilles et al., 2000). Mineralised veins are typically thin (< 0.5 cm) sheeted arrays and stockworks containing quartz–pyrite–chalcopyrite ± bornite ± molybdenite ± calcite (Fig. 2R).

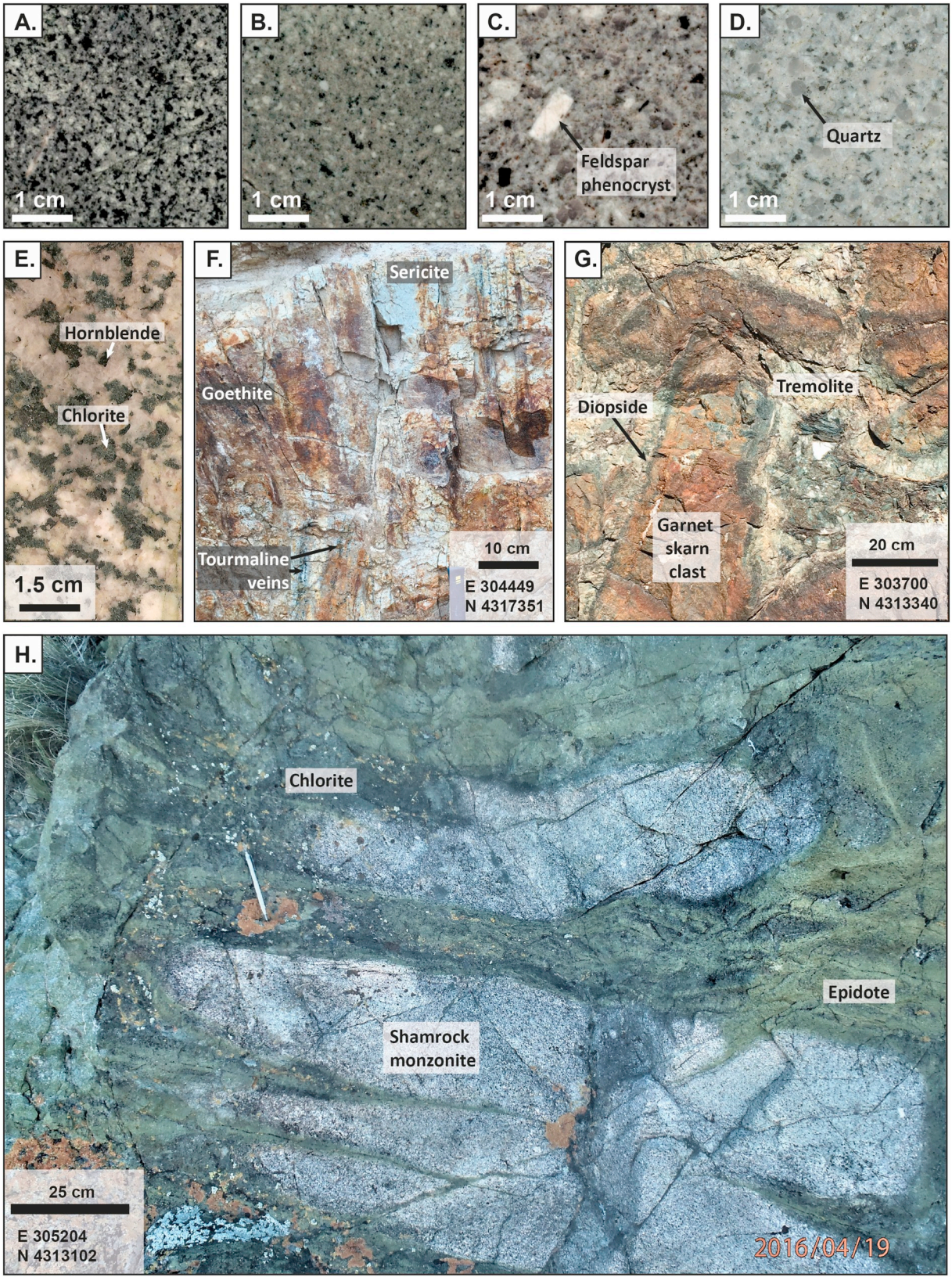

(caption on next page)

Fig. 2. Primary rock types and key alteration features from Yerington, Nevada. A – E: Primary intrusive rock types: A. McLeod Hill monzodiorite; B. Bear quartz monzonite; C. Luhr Hill granite with feldspar phenocrysts; D. Quartz-phyric Luhr Hill granite porphyry dyke; E. Shamrock monzonite. F – R: Key alteration features: F. Thin (< 0.5 cm -wide) sheeted tourmaline veins in a strongly Fe-oxide and sericite-altered Luhr Hill porphyry dyke; G. Garnet skarn clasts in diopside–-tremolite–calcite-cemented breccia from the Casting Copper skarn; H. Strong epidote alteration along the northern contact of the Shamrock monzonite; I. Pervasive epidote–chlorite–actinolite alteration in the Shamrock monzonite; J. Epidote vein with epidote–albite vein halo in McLeod Hill monzodiorite; K. Epidote vein with albite–epidote–chlorite vein halo in McLeod Hill monzodiorite; L. Epidote vein with epidote–albite vein halo in Shamrock monzonite; M. Epidote clots with albite alteration halos in McLeod Hill monzodiorite; N. Epidote clot with albite alteration halo in Bear quartz monzonite; O. Thin (< 1 cm-wide) epidote and quartz vein with wide (> 10 cm) albite vein halo in McLeod Hill monzodiorite. P. Secondary biotite alteration and disseminated pyrite in Luhr Hill granite porphyry dyke; Q. Epidote pseudomorphs of feldspar phenocrysts in Luhr Hill granite porphyry dyke; and R. Quartz–chalcopyrite–epidote–calcite–chlorite vein in Luhr Hill granite porphyry dyke. Sample IDs are shown where the photograph is representative of the hand sample sent for whole rock geochemistry analysis. UTM coordinates for picture locations are provided in NAD83 Zone 11N.

2.2. Skarn deposits of the Ann Mason fault block

The Casting Copper Cu-skarn deposit and the Ludwig Cu-deposit occur within a kilometre of the southern contact of the Yerington batholith (Fig. 1; Harris and Einaudi, 1982). The host rocks are dominantly Triassic and Jurassic limestone of the Mason Valley and Ludwig Formations (Harris and Einaudi, 1982; Proffett and Dilles, 1984). These deposits are characterised by several features (Einaudi, 1977; Harris and Einaudi, 1982): (1) a mineral assemblage consisting primarily of andradite garnet and pyroxene replaced by a later assemblage of apatite–quartz–sulfide; (2) relatively low total sulfides, generally < 5 vol%; (3) chalcopyrite to pyrite ratios generally > 10; (4) absence of magnetite or hematite; (5) a gangue mineralogy dominated by andradite; (6) strong brecciation (Fig. 2G); and (7) formation depths of approximately 2 km.

Previous workers have proposed a genetic relationship between the Yerington batholith and the skarn deposits due to the porphyry-style mineralisation hosted in the Yerington batholith and the development of endoskarn in the McLeod Hill monzodiorite (Knopf, 1918; Einaudi, 1977; Harris and Einaudi, 1982). The Shamrock batholith contains no known porphyry-style mineralisation and only minor endoskarn (garnet–pyroxene) development. Strong epidote-chlorite alteration is developed along the northern contact of the Shamrock batholith with Triassic sedimentary rocks (Fig. 2H), and it is possible that some exoskarn alteration developed in the Triassic sedimentary host rocks is related to the Shamrock batholith, given the proximity of the batholith to skarn deposits, such as Casting Copper (Fig. 1).

2.3. Alteration in the Ann Mason fault block

The main porphyry-Cu mineralisation event at the Ann Mason deposit is associated with potassic alteration (Fig. 2P), consisting of biotite ± K-feldspar, and occurs in a restricted domain in the deposit core (Dilles and Einaudi, 1992). A later quartz–sericite–pyrite alteration assemblage occurs above and adjacent to Ann Mason and comprises fine-grained muscovite–quartz–pyrite ± rutile ± tourmaline ± illite (Fig. 2F; Dilles and Einaudi, 1992; Watkins et al., 2015). Epidote-bearing alteration assemblages in the Yerington district are widespread throughout the Yerington and Shamrock batholiths (Harris and Einaudi, 1982; Carten, 1986; Dilles and Einaudi, 1992; Dilles et al., 1992; Dilles et al., 2000; Cohen, 2011). Previous workers separate regionally dominant epidote-bearing assemblages into a sodic-calcic group and a propylitic group (Carten, 1986; Dilles and Einaudi, 1992; Dilles et al., 1995).

Sodic-calcic alteration was first defined by Carten (1986) at the Yerington deposit, Yerington district as the assemblage quartz–oligoclase–titanite–rutile–apatite ± epidote ± actinolite. The assemblage was characterised by the conversion of magmatic minerals to more Na- or Ca-rich minerals including the replacement of K-feldspar by oligoclase and of biotite by actinolite. At the Ann Mason deposit, Dilles and Einaudi (1992) and Dilles et al. (1995) characterised the assemblage as: (1) the addition of Na, and K-feldspar replaced by Na-plagioclase or epidote; (2) the replacement of hornblende and biotite by actinolite; (3) an occurrence restricted to between 3.5 and 6 km paleodepth; (4) structurally controlled along the contact between the McLeod Hill monzodiorite and the Luhr Hill granite cupola, and along the axis of the Luhr Hill granite dyke swarm (Fig. 1); and (5) having formed from non-magmatic hypersaline brine, as interpreted using radiogenic whole-rock $^{87}Sr/^{86}Sr$ values. In contrast, propylitic alteration around the Ann Mason deposit was described by Dilles and Einaudi (1992) and Dilles et al. (1995) as: (1) characterised by weak alteration of plagioclase to albite–epidote–sericite; (2) replacement of hornblende by actinolite and of biotite by chlorite–rutile; (3) an occurrence restricted to shallow paleodepths, < 4 km; (4) no specific structural controls related to lithological contacts; and (5) formed from a magmatic-dominant hydrothermal fluid as evidenced by δ18O values magmatic fluid source.

Battles (1990) identified four key alteration assemblages in the exposures of Shamrock monzonite in the Ann Mason fault block: (1) biotite–magnetite, which occurs in the northern part of the batholith; (2) actinolite ± pyroxene ± epidote, which is the most common style of alteration and altered up to 50% of rocks; (3) epidote–albite–actinolite ± scapolite ± apatite (sodic-calcic alteration), that has altered rocks predominantly along the northern contact of the Shamrock batholith with host sedimentary and volcanic rocks; and (4) minor albite.

Field observations from the Ann Mason deposit centre, made during our study, indicate epidote occurs as part of thin veins in the assemblage: epidote–quartz–chlorite–pyrite–albite ± calcite (Fig. 2R). Chlorite typically occurs as the partial replacement of biotite, actinolite, and/or hornblende (Fig. 2R). In the deep parts of the Yerington batholith (> 4 km paleodepth), epidote occurs as anhedral clots with albite–actinolite alteration halos (Fig. 2M and N). Outside the Ann Mason deposit centre, in the shallow parts of the Yerington batholith (< 3.5 km paleodepth), epidote typically occurs as thin veins (< 1 cm) with albite–epidote–chlorite vein halos (Fig. 2J and K; 2O). In the Shamrock monzonite, along the northern contact with host Triassic to Jurassic volcanic and sedimentary rocks, semi-massive to massive epidote (± actinolite ± chlorite) veining is common (Fig. 2H and I). Similar to the distal fringes of the Yerington batholith, epidote also occurs as veins with albite–epidote vein halos in the central parts of the Shamrock batholith (Fig. 2L).

3. Methods

3.1. Whole-rock geochemistry

A total of 154 chip and drill core samples of igneous rocks (McLeod Hill monzodiorite, Bear quartz monzonite, Luhr Hill granite and associated dykes, Shamrock monzonite) were analysed for their major and trace-element chemical composition. Sample locations are shown in Fig. 1. Whole-rock chemical analyses were completed at Bureau Veritas Mineral Laboratories, Vancouver, Canada. Samples were dried at 105 °C prior to crushing. Loss on ignition (LOI) was calculated from changes in sample weight before and after a series of step-heating measurements. Samples were jaw-crushed, split, and pulverised to < 0.074 mm diameter. A total of 43 major and trace elements were analysed using lithium borate fusion package LF200 (http://acmelab.com/services/). A 0.2 g powdered sample was fused in a graphite crucible with 1.5 g of

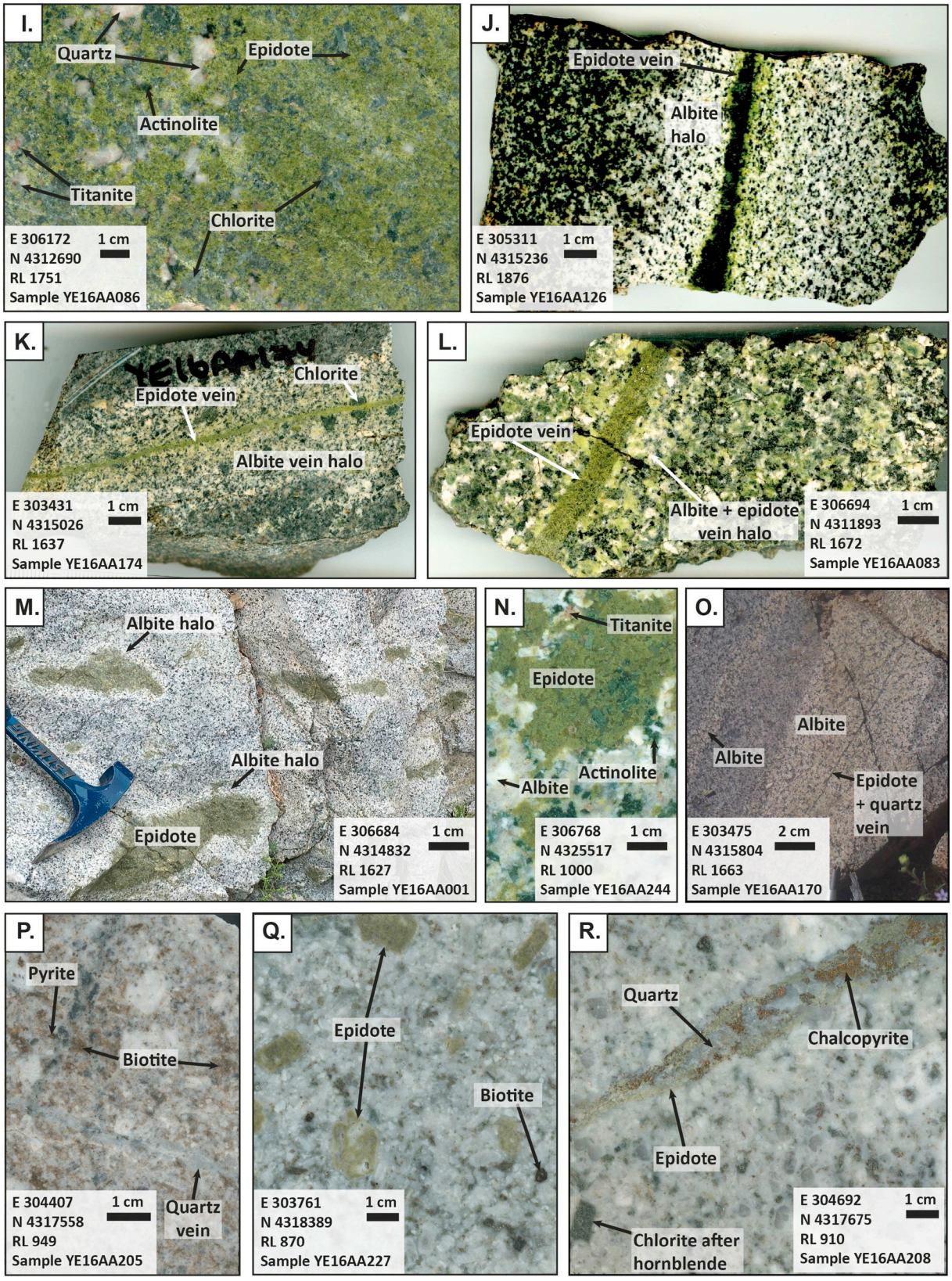

Fig. 2. (*continued*)

$LiBO_2/LiB_4O_7$ flux at 980 °C for 30 min and then dissolved in 5% HNO_3. Major elements were determined using a Jarrel Ash AtomComp Model 975/Spectro Ciros Vision inductively coupled plasma emission spectrograph. Trace elements were analysed using a Perkin-Elmer Elan 6000 or 9000 inductively coupled plasma mass spectrometer. Laboratory quality assurance and quality control procedures were employed with digested standards run every 68 samples, and a digestion duplicate run every 15 samples, with recalibration of the instrument every 68 samples. Carbon and sulfur were analysed by the Leco method (TC003).

3.2. Least-altered univariate element values and calculation of a geometric mean for major rock units

Porphyry-Cu deposits typically have large alteration footprints that can extend kilometres from the deposit centre (Lowell and Guilbert, 1970; Gustafson and Hunt, 1975; Seedorff et al., 2005; Sillitoe, 2010; Cooke et al., 2014a). While the use of unaltered samples for mass balance calculations is ideal, identifying samples of unaltered protolith rocks can be difficult due to this regional-scale pervasive alteration. In the Yerington district, samples available at surface are variably hydrothermally altered, and/or locally affected by surface weathering. As such, a suite of least-altered samples were identified based on a number of key parameters: (1) containing the lowest degree of weathering and alteration minerals, as determined by hand sample inspection compared to other rocks in the same lithological unit; (2) exhibiting < 1.5 wt% loss on ignition; (3) plotting within the least-altered domain of the alteration box plot diagram (Large et al., 2001; Fig. 3); and (4) plotting in the same rock type classification diagram fields as least-altered samples from Dilles (1987). Appendix B contains major and trace element concentrations of least-altered samples for each of the four major rock units: Luhr Hill granite, Bear quartz monzonite, McLeod Hill monzodiorite, and Shamrock monzonite.

3.3. Isocon diagrams

Gresens' (1967) equation, rearranged by Grant (1986; Eq. (1), Table 1), calculates relative gains and losses of mobile elements based on the numerical displacement of data points from a reference isocon line. The position of the isocon is determined using a suite of immobile elements, e.g., TiO_2, P_2O_5, Al_2O_3, and Zr (Floyd and Winchester, 1978). These elements are considered immobile if they lie along a common linear trend, typically fitted by eye according to the Grant (1986) approach (Fig. 4). Element ratios of least-altered samples to altered samples are ratioed against the whole-rock isocon value. C^A/C^O values < 0 indicate depletion and values > 0 indicate mass addition. M^A/M^O values > 1 indicate overall mass addition and values < 1 indication overall mass removal.

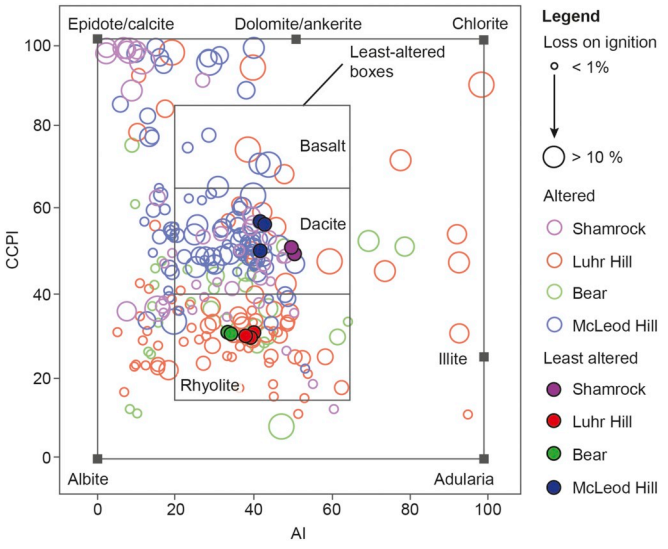

Fig. 3. Whole-rock geochemical data showing altered and least-altered igneous samples from Yerington district, plotted on the alteration box diagram of Large et al. (2001). Mass balance calculations presented in this study include only igneous units from the Ann Mason fault block. CCPI (chlorite–carbonate–pyrite index) = 100 (MgO + FeO) / (MgO + FeO + Na_2O + K_2O). AI (Ishikawa's Alteration Index) = 100 (K_2O + MgO) / (K_2O + MgO + Na_2O + CaO).

Table 1
Description of variables comprising Eq. (1). Modified from Grant (1986).

Variable	Description
C^A	Final concentration of an element in an altered rock
C^O	Final concentration of an element in the least-altered rock
M^A	Mass of altered rock
M^O	Mass of least-altered rock
Ci^A	Initial concentration of element in altered rock
Ci^O	Initial concentration of element in least-altered rock
C^A/C^O	Change in concentration (addition or depletion) of an element between altered and unaltered sample pair. To obtain% mass change, multiply C^A/C^O by 100.
M^A/M^O	Isocon reference line calculated from changes
Ci^A/Ci^O	Initial concentration of an element in the altered sample ratioed to an unaltered sample

$$\frac{C^A}{C^O} = \left(\frac{M^A}{M^O}\right) * \left(\frac{Ci^A}{Ci^O}\right) - 1 \quad (1)$$

A rock unit or alteration domain is naturally heterogeneous, meaning that elemental concentrations span a range of values (Vistelius, 1960; Allegre and Lewin, 1995; Monecke et al., 2005). Therefore, problems arise when selecting single representative samples of unaltered or protolith rock with which to assess mass changes using Grant's (1986) isocon method. The issue of geochemical heterogeneity with respect to mass balance calculations can be addressed by representing variability as a threshold envelope around the isocon (Fig. 4). This envelope bounds the variance of immobile element data points around the isocon. Any mobile element data points within the envelope of uncertainty cannot reliably be interpreted as added or removed and are referred hereafter as having no net change. Numerically, this envelope is calculated by taking the maximum and minimum values of immobile element sample pairs used in the isocon, i.e. min, max (C^A/C^O TiO_2; C^A/C^O P_2O_5; C^A/C^O Zr; C^A/C^O Al_2O_3).

The benefit of defining an envelope of uncertainty is that the natural variation, both spatially and chemically, in least-altered sample suites can be quantified. Because mass balance calculations rely on the characterisation of least-altered samples, there is an assumption that the defined least-altered sample suite represents a single rock type that does not change over a large spatial area (e.g., over several kilometres), an assumption not compatible with the natural heterogeneity inherent to an intrusive unit (Vistelius, 1960; Reimann and Filzmoser, 2000). The envelope of uncertainty allows addition and depletion to be identified outside the natural variability in the lithological unit defined by the least-altered samples.

Previous mass balance work from the Ann Mason deposit by Cohen (2011) used isocon diagrams to compare the concentration of trace elements in chlorite and muscovite relative to whole-rock geochemical analyses. These mass balance results were used to identify the contribution of elements hosted in different minerals, using whole-rock geochemical analyses, but these data were not examined spatially. Battles (1990) evaluated the addition and depletion of elements in a limited number of samples from the Shamrock monzonite. Elements were normalised to Al_2O_3 or Zr, and results were used to assess chemical changes between rocks from five key alteration assemblages and unaltered Shamrock monzonite. Battles (1990) concluded however, that protolith samples selected for some alteration groups were not optimal.

3.4. Isocon diagrams applied to a 2-D dataset

Most previous studies have applied isocon diagrams (or mass balance calculations) to a restricted number of sample pairs to explain the behaviour of elements on a deposit scale, as a general comparison of alteration zones (e.g., Grant, 1986; Battles, 1990; Huston, 1993; Cooke

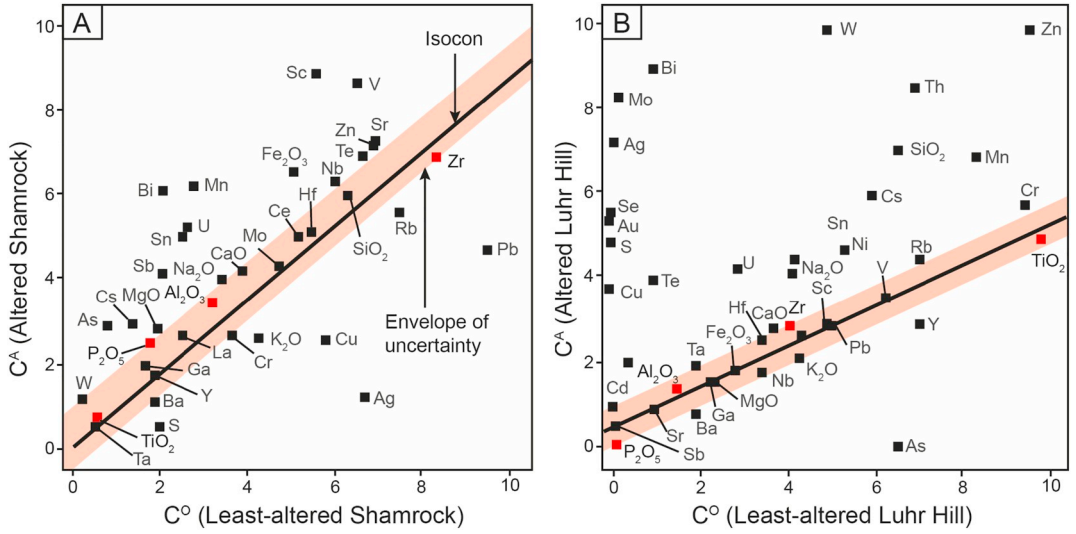

Fig. 4. Isocon diagram (based on Grant, 1986) for: A. Least-altered Shamrock sample YE17AA069 vs. altered Shamrock sample YE16AA112. B. Least-altered Luhr Hill sample YE17AA038 vs. altered Luhr Hill sample YE16AA208. The dark black line denotes the isocon, a line of constant no net mass change (Grant, 1986). The orange shaded area defines the envelope of uncertainty, which is bounded by the maximum and minimum values of selected immobile elements.

et al., 1998; Waters, 2001; Rolland et al., 2003; Sturm, 2003; Cohen, 2011; Villaplaza et al., 2017). Here, we calculate mass addition and depletion using the isocon method for a dataset of 154 samples and present the mapped results in 2-D space across the Ann Mason deposit. While technological advances have been made by developing computer programs to automate mass balance calculations for ease of viewing in graphical space (e.g., Sturm, 2003; Coelho, 2006; Lopez-Moro, 2012; White, 2017), we are not aware of the results from these programs being illustrated in map-space in the published literature.

Each of the following steps was completed as a separate worksheet in Microsoft Excel (products.office.com), for each major igneous rock unit: (1) two to four least-altered samples (McLeod Hill monzodiorite: $n = 3$; Bear monzonite: $n = 2$; Luhr Hill granite and associated dykes: $n = 3$; and Shamrock monzonite: $n = 2$) were identified from the larger whole-rock geochemistry dataset based on the criteria outlined in Section 3.2; (2) least-altered geometric mean values were calculated for all elements in each suite of least-altered samples (see Appendix B); (3) ratios were calculated between altered samples and least-altered geometric means for all elements (Ci^A/Ci^O); (4) median values between immobile elements TiO_2 and Zr were calculated for each sample pair (altered sample versus least-altered geometric mean) to determine the isocon value (M^A/M^O); (5) values calculated in Step 4 were ratioed to the isocon and 1 was subtracted; and (6) the envelope of uncertainty was selected using variability of the immobile elements Ti and Zr. The 2nd and 3rd quartile values of Ci^A/Ci^O (Ti and Zr) correspond to a range from −0.25% mass depletion to +0.25% mass addition. Major element addition and depletion values were calculated using element-oxide concentrations but are referred to in the text in element form (i.e. Ca or calcium, not CaO or calcium-oxide).

3.5. Appropriate elements for mass balance assessment

Not all elements are appropriate for mass balance calculations. When the method was first developed, mass balance calculations were applied to study bulk changes of major elements between alteration domains, not trace element chemistry (Riverin and Hodgson, 1980; Grant, 1986; White et al., 2016). This restriction was applied because the concentrations of many trace elements were near or below detection limit. Calculations that result in net addition of these elements are generally accurate, but depletion cannot be accurately represented. This occurs because theoretically an element can be added to a rock until that rock is comprised of only that element, and the concentration of that element in the rock is 100%. Conversely, a sample cannot be infinitely depleted of an element, only depleted of the small concentration of the element that is present in the background rocks. The result is an over representation of the addition of elements, particularly trace elements in a rock, as compared to the removal of those same elements.

It is not possible to fully remove the over representation of addition as compared to depletion of trace elements; however, here we offer recommendations that can be applied to any element in a whole-rock geochemistry dataset, for a given rock type. The purpose of these recommendations is to determine if the data distribution for that element is statistically robust to undergo mass balance calculations. These recommendations were informed by Martín-Fernández et al. (2012) and Gazley et al. (2015) and use a box and whisker plot as a visual assessment of the compatibility of a geochemical dataset for mass balance calculations. Plots of eight elements used in this study are shown in Fig. 5. Values below the detection limit in the dataset were assigned a value of half the instrumental detection limit. For element data to satisfy the requirements of statistical robustness for our purposes, two criteria must be met. For the first criteria (1) the majority of data (2nd and 3rd quartile boxes on the box and whisker plot) should be at least an order of magnitude above the detection limit. This ensures that the mass balance calculations can accurately represent depletion up to an order of magnitude below least-altered values. If, however, this is not the case, and the geometric mean of least-altered samples is at the detection limit (e.g., Mo; Fig. 5B), such elements can still be used to accurately assess addition, but not depletion. For the second criteria (2), the variation in the element values of each sample that make up the least-altered geometric mean should occur well within the bounds of the 2nd and 3rd quartile boxes. Examples of elements that do not meet these criteria include Hg (Fig. 5A), Te, Sn, and the rare earth elements. In Fig. 5, variation is represented as one standard deviation from the geometric mean of a least-altered sample. Significant variation between the original composition of least-altered samples makes it difficult to determine whether calculated addition or depletion is accurate or related to natural variability in rock type.

4. Results

4.1. Addition and depletion patterns around the Ann Mason deposit

Examples of traditional isocon diagrams, using sample pairs from

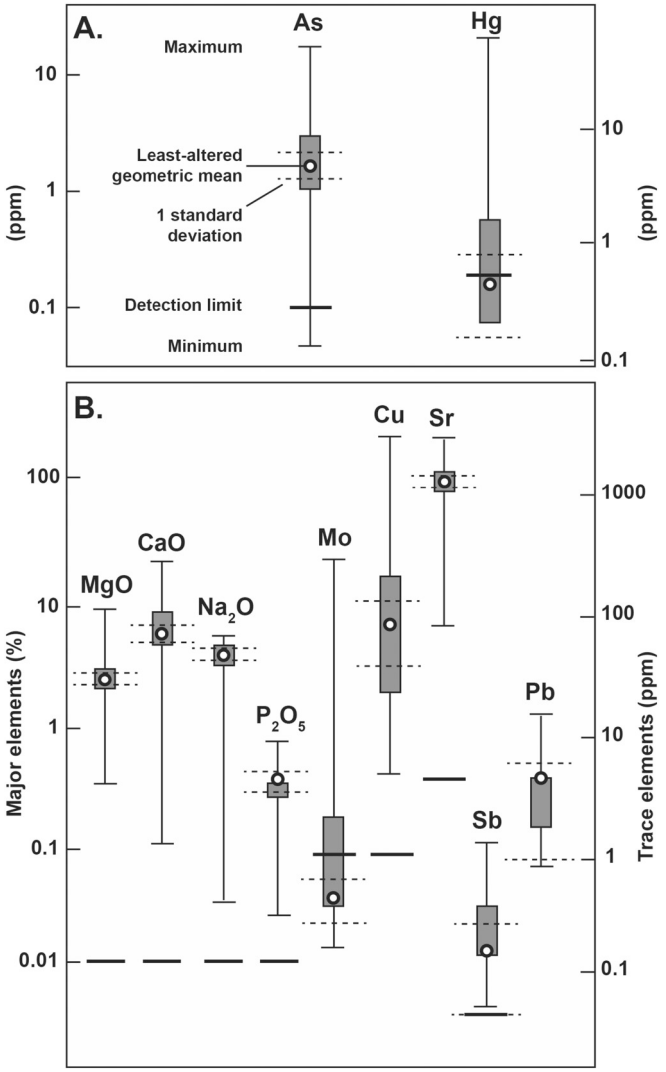

Fig. 5. Box and whisker plots of elements used for mass balance calculations in this paper (As, MgO, CaO, Na_2O, Mo, Cu, Sr, and Sb) and an example of an element not suitable for mass balance calculations (Hg). A. As and Hg; B. Major element oxides MgO, CaO, Na_2O, P_2O_5, and trace elements Mo, Cu, Sr, Sb, and Pb. Detection limit for Pb is 0.01 ppm. Dataset is from the McLeod Hill monzodiorite; $n = 80$. Labels on the plot of As apply to all other box and whisker plots. Minimum and maximum refer to respective values for a given element. Minimum values can occur below the detection limit if a sample returned a value less than the detection limit as half the detection limit value was used as a substitution. One standard deviation refers to the standard deviation from the least-altered geometric mean of samples in the least-altered suite.

the Yerington district, are shown in Fig. 4. Table 2 contains petrographic descriptions for the samples presented in Fig. 4. The isocon diagram for epidote–albite-altered Shamrock monzonite (YE16AA112) relative to least-altered Shamrock monzonite (YE17AA068; Fig. 4A) shows minor addition (Fe_2O_3, Sr, Mn, Bi, V, U, As, Sb, Sn, W, and Sc) and depletion (K_2O, Cu, Pb, Ag, and S). These changes are associated with epidote–chlorite veins and pervasive epidote–albite–chlorite alteration developed in the altered sample (YE16AA112; Table 2). Most data points for these samples cluster within the isocon envelope and indicate relatively minor mass increase in the altered sample relative to the protolith sample (isocon slope = 0.87). In contrast, the isocon diagram for the Luhr Hill samples (Fig. 4B) shows significant addition of elements (Cu, Ni, S, Se, Au, Ag, Mo, Zn, SiO_2, Mn, Bi, W, Cd, Th, Te, and U), and loss of only a few elements (As, Y, Ba). The addition of these elements is related to the presence of a Cu—Mo bearing vein in the altered sample (YE16AA208; Fig. 2R; Table 2). The altered sample shows overall mass gain relative to the least-altered reference sample. The slope of the isocon is 0.54, indicating an approximately 46% addition of mass during alteration.

Fig. 6 presents calculated mass change results for Ca, Mg, Na, P, Sr, Cu, Mo, Sb, As, and Pb. Table 3 outlines the threshold values used to separate mass change results into four categories: depletion, no net change, weak addition, and strong addition. We use these numerical categories to evaluate quantitatively patterns of addition and depletion around the Ann Mason deposit. These categories are numerically similar to those devised by Huston (1993) but do not have a subdivided depletion category (weak vs. strong) due to the limitations imposed by analytical detection limits.

Calculated results for Ca (Fig. 6A) and Sr (Fig. 6J) define similar addition and depletion patterns within the Yerington batholith and around the Ann Mason deposit. Values are mixed (both added and depleted) in the centre of the Ann Mason deposit and the underlying Luhr Hill cupola, though Ca and Sr depletion dominate. Samples from the Blue Hill deposit, west of the Ann Mason deposit (shallower paleodepth) and in a different fault block, show variable mass change in Ca (−68 to 47%) and Sr (−44 to 52%). Calcium and Sr were added outside of the Ann Mason deposit (Ca up to 1570%; Sr up to 315%). The majority of samples from the southern and central parts of the Shamrock batholith show no net change (−25 to 25%), only weak addition of Ca and Sr. There are, however, zones of stronger Ca addition (up to 554%) and Sr addition (up to 514%) at the northeastern contact of the Shamrock intrusion with host volcanic and sedimentary rocks, and the western margin of the batholith. Calcium was also strongly added to a sample of the Shamrock monzonite (YE16AA063; 196% Ca addition) adjacent to the Casting Copper skarn. Carbonate rocks, the primary hosts to Cu mineralisation at the Casting Copper and Ludwig deposits, were not sampled as part of this study. As such, mass balance calculations were not performed on samples associated with Cu-mineralisation at either deposit.

Table 2
Petrographic descriptions of samples presented in the isocon diagrams from Fig. 4.

Sample ID	Easting	Northing	Elevation (m)	Rock unit	Rock type	Alteration		Vein	
						Minerals	Style and intensity	Minerals	Description and abundance
YE17AA069	303,185	4,311,691	1662	Shamrock	Monzonite	Albite	Disseminated; trace	Epidote	Planar; < 1%
YE16AA112	305,203	4,313,378	1913	Shamrock	Monzonite	Epidote– albite–chlorite	Pervasive; moderate	Epidote– chlorite	Stockwork; 30%
YE17AA038	309,109	4,312,601	1416	Luhr Hill	Granite porphyry dyke	Epidote	Replacement of hornblende and biotite; trace		
YE16AA208	304,692	4,317,675	910	Luhr Hill	Granite porphyry dyke	Epidote – quartz–chlorite	Replacement of hornblende and biotite; weak; pervasive silicification; moderate	Epidote– quart–calcite –chlorite –chalcopyrite	1 cm wide; planar; 15%

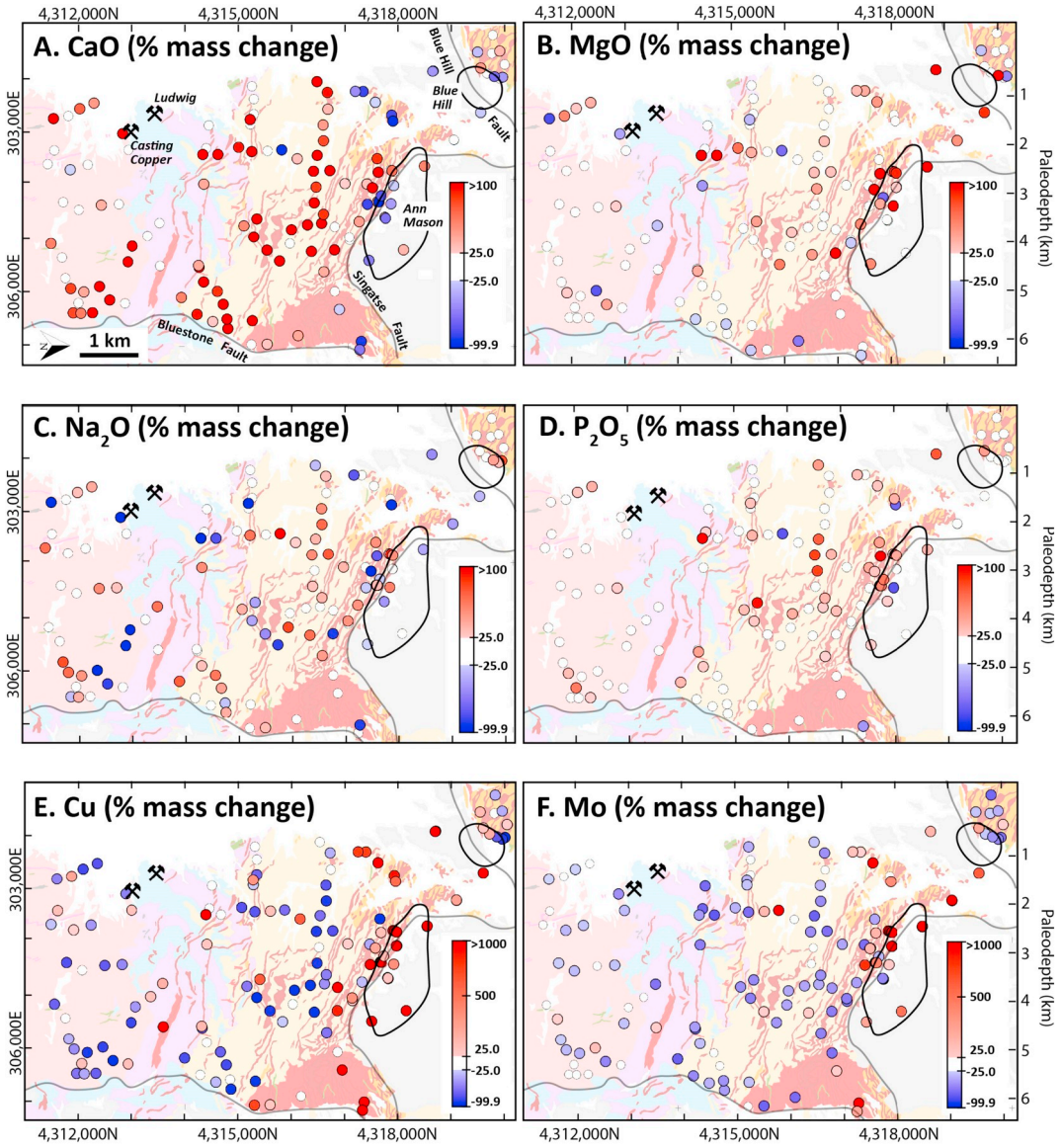

Fig. 6. Geology map modified from Proffett Jr. and Dilles (1984) showing calculated addition and depletion results normalised to protolith for: A. CaO; B. MgO; C. Na_2O; D. P_2O_5; E. Cu; F: Mo, G. Sb; H. As; I. Pb; and J. Sr; (n = 154). Estimated paleodepths modified from Dilles and Einaudi (1992) are shown. Thick black lines indicate 0.1% Cu shells projected to surface for the Ann Mason and Blue Hill deposits. Major faults are shown by grey lines. UTM coordinates shown are in NAD83 Zone 11N. Legend bins (% mass change) are those outlined in Table 3. Calculated values for a given element that plot within the envelope of uncertainty (Fig. 4) are shown as white circles. Blue hues indicate depletion while warm colors (red) reflect elements added relative to protolith composition. The legend is skewed towards addition due to the factors discussed in Section 3.5. (For interpretation of the references to colour in this figure legend, the reader is referred to the web version of this article.)

Magnesium (Fig. 6B) has been added to the central and shallow parts of the Ann Mason deposit (up to 870%). West of the deposit centre, in the shallow paleoenvironment, Mg has been weakly added to some rocks (< 60%). In the deep paleoenvironment, east of the deposit centre, Mg depletion is more prevalent (up to −63%), or samples record no net change in Mg (−25 to 25%). Two samples of Luhr Hill porphyry dyke that have intruded Triassic sedimentary and volcanic rocks show Mg addition (up to 1100%). Sample YE16AA063, Shamrock monzonite adjacent to the Casting Copper skarn, records Mg depletion (−45). Overall, samples from the central parts of the Shamrock batholith record no net change in Mg (−25 to 25%). Samples from the western, northern, and eastern parts of the batholith record both addition and depletion (−82 to 58%).

Sodium addition and depletion patterns are highly variable (Fig. 6C). Samples from the deep (eastern) parts of the Yerington batholith show addition (25 to 75%), or no net change in Na (−25 to 25%). The majority of samples from the Blue Hill deposit show overall no net change (−25 to 25%), or weak addition (< 80%). In the core of the Ann Mason deposit, addition and depletion values are mixed (−98 to 93%). In the shallow (western) parts of the Yerington batholith, outside the deposit centre, Na has been added to most samples (up to 136%). Samples from the central part of the Shamrock batholith show overall no net change in Na (−25 to 25%), while samples on the margins of batholith show variable addition and depletion of Na (−98 to 80%). Sodium depletion (Fig. 6C) in in the Shamrock batholith is associated with strong Ca addition (Fig. 6A).

Phosphorus has been added (25 to 458%) to samples from the region in and around the Ann Mason deposit centre, and to the shallow, more deposit distal parts of the Yerington batholith (< 4 km paleodepth). Most samples from the deep parts of the Yerington batholith (> 4 km paleodepth) record no net change in P (−25–25%). Similarly, samples from the central parts of the Shamrock batholith show no

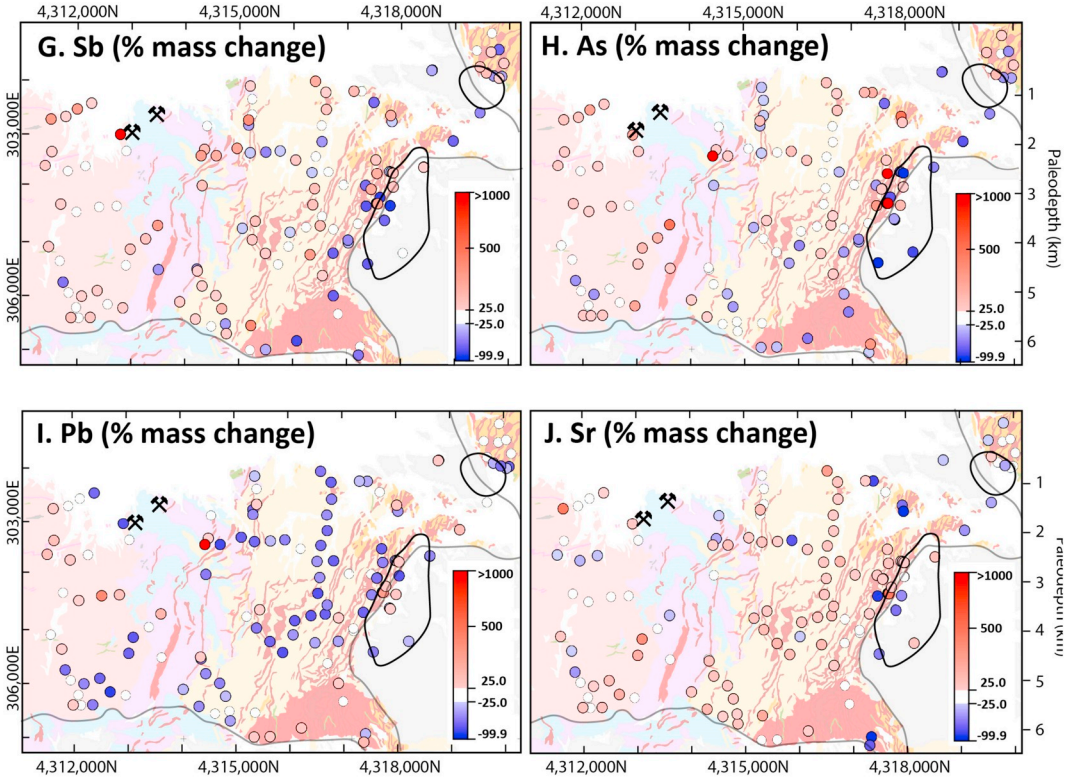

Fig. 6. (*continued*)

Table 3
Calculated results binned into four categories that reflect the amount of mass change.

Element	% Mass change			
	Depletion	No net change	Weak addition	Strong addition
CaO	−99.9 to −25	−25 to 25	25 to 100	> 100
MgO	−99.9 to −25	−25 to 25	25 to 100	> 100
Na_2O	−99.9 to −25	−25 to 25	25 to 100	> 100
P_2O_5	−99.9 to −25	−25 to 25	25 to 100	> 100
Pb	−99.9 to −25	−25 to 25	25 to 1000	> 1000
Sr	−99.9 to −25	−25 to 25	25 to 1000	> 1000
Cu	−99.9 to −25	−25 to 25	25 to 1000	> 1000
Mo	−99.9 to −25	−25 to 25	25 to 1000	> 1000
As	−99.9 to −25	−25 to 25	25 to 1000	> 1000
Sb	−99.9 to −25	−25 to 25	25 to 1000	> 1000

strong addition or depletion (−25–25%). Seven samples from the northern, western, and eastern margins of batholith record weak addition (< 63%). Samples that record P addition in the Shamrock batholith also record Ca and Na addition (Fig. 6A and C).

Copper (Fig. 6E) shows strong addition (up to 95,000%) at the Ann Mason deposit, and down to 6 km paleodepth in the cupola region below the porphyry deposit. Copper addition is most laterally extensive at shallow depths, close to 1 km paleodepth (up to 23,200%). Outside the Ann Mason deposit centre and Luhr Hill cupola, Cu has been removed from country rocks (up to −96%), including samples from both McLeod Hill monzodiorite and Luhr Hill granite porphyry dykes. One sample of Luhr Hill porphyry dyke (YE16AA046) that has intruded Triassic sedimentary rocks shows strong Cu addition (up to +1150%). Samples of Shamrock monzonite outside the Casting Copper skarn show variable Cu addition and depletion (−60% and 116%). Copper has been depleted from most samples in the Shamrock batholith (approaching −100%). Nine samples from the Shamrock batholith show weak addition (up to 270%).

Molybdenum (Fig. 6F) has a similar but more varied addition and depletion pattern compared to Cu. Molybdenum is weakly to strongly added (up to 10,500%) in the core of the Ann Mason deposit and down through to the Luhr Hill cupola. Many data points outside the deposit centre record depletion, or no net change of Mo (−25 to 25%). Samples from the Shamrock batholith show either little overall net addition or loss of Mo (−25 to 25%), or weak Mo addition or depletion (−66 to 130%).

Addition and depletion patterns for Sb (Fig. 6G) and As (Fig. 6H) are opposite to both Cu and Mo mass change patterns in the Yerington batholith. Antimony and As have been removed in the core of the Ann Mason deposit (up to −92% Sb; up to 95% As) and, down through the Luhr Hill cupola region (up to −84% Sb and Sb) at ~6 km paleodepth. These elements have also been added both inside and outside of the deposit centre (up to 414% Sb up to 1900% As). Sample YE16AA046, Luhr Hill porphyry dyke that has intruded sedimentary rocks, records the highest addition of As (5200%). This As addition is associated with strong Ca, Mg, P, and Pb addition. Antimony has been strongly added to one sample (YE16AA063) from outside Casting Copper skarn deposit (1100%). Addition of Sb in this sample coincident with Ca addition and Na, Cu depletion. Mass changes in Sb and As are varied in the Shamrock batholith. Antimony and As have been weakly added ore removed (−66 to 343% Sb; −52 to 560% As) or show no net change (−25 to 25%) in samples from the Shamrock batholith.

Lead (Fig. 6I) has been weakly added (up to 320%) to a restricted suite of samples in the Luhr Hill cupola, the deposit centre, and the Blue Hill deposit. Samples in both the deep (> 4 km paleodepth) and shallow parts (< 4 km paleodepth) of the Yerington batholith, outside the deposit centre, record Pb depletion (up to −83%). One Luhr Hill dyke sample that intruded the Triassic volcanic-sedimentary rocks (YE16AA046) records strong Pb addition (5400%). Lead has been weakly added (up to 430%) to samples from the central and western (shallow) parts of the Shamrock batholith. Conversely, samples from the eastern (deeper) parts of the batholith, record more consistent Pb depletion (up to −90%).

5. Discussion

5.1. Addition and depletion patterns as proxies for mineral reactions

Depletion of Ca in the centre of the Ann Mason deposit (Fig. 6A) is likely due to the destruction of Ca-feldspar and Ca-amphibole, and the formation of K-feldspar, sericite, and/or kaolinite in the potassic, phyllic, and/or argillic alteration zones. This is consistent with our petrographic observations, which show that the area immediately adjacent to the Ann Mason deposit is characterised by strong sericite–pyrite (or goethite) alteration (Fig. 2F). Similar element patterns are typical in other Cu−Au deposits (e.g., Highland Valley, Olade and Fletcher, 1976; Panguna, Ford, 1978; and Bajo de la Alumbrera, Ulrich and Heinrich, 2002). In these deposits, Sr, Na and Ca were removed from the core of the system, and correspond to strong potassic alteration and plagioclase destruction.

Distal to the Ann Mason deposit, amphibole and plagioclase are replaced by epidote (and minor chlorite) in the propylitic alteration domain, and Ca has been added to rocks (Fig. 2J and K). Calcium and Sr addition are also observed along the northern contact of the Shamrock intrusion (Fig. 6A and J) where the Shamrock intrusion is in contact with carbonate-bearing sedimentary and volcanic rocks (Fig. 1). This Ca addition is associated with abundant, cross-cutting epidote veins with pervasive epidote and chlorite alteration (Fig. 2H). The correlation between Sr and Ca addition associated with epidote alteration is consistent with results from Battles (1990). Conversely, unlike the results of Battles (1990), Shamrock samples with strong Ca addition show either no net change in Na (−25 to 25%) or Na depletion (Fig. 6C). The lack of significant Na addition suggests that these samples from the northern contact of the Shamrock batholith are not part of the sodic-calcic alteration assemblage described by Battles (1990) or Carten (1986). Instead, this alteration is more likely related to endoskarn processes developed during emplacement of the Shamrock batholith adjacent to carbonate-bearing wall rocks.

Strontium addition and depletion patterns, which are similar to Ca, are positively correlated with the intensity of epidote alteration. Homovalent cation substitutions are common in epidote; in this case, Sr^{2+} would substitute for Ca^{2+} in the A2 site (Armbruster et al., 2006). While Sr can partition into calcite, a common constituent of the propylitic alteration assemblage, our observations indicate calcite alteration is minor compared to epidote alteration.

The Ann Mason deposit contains a zone of strong Mg addition (Fig. 6B), likely related to the replacement of biotite, hornblende, and actinolite by chlorite. Chlorite replacement of mafic minerals is common across the Yerington batholith (Fig. 2K and Q). The absence of strong Mg addition (> 100%) outside the Ann Mason deposit, as might be expected with a propylitic (epidote–chlorite) alteration halo, is consistent with visual observation of the samples, which show veins dominated by epidote and only minor chlorite. The replacement of Mg-bearing minerals like hornblende and actinolite by chlorite, outside the deposit centre, would result in the observed weak Mg addition pattern.

As expected, the centre of the Ann Mason deposit is characterised by strong Cu and Mo addition (Fig. 6E and F). Copper and Mo addition is laterally restricted (< 1 km) but vertically extensive (up to 6 km). These results are consistent with Cu and Mo dispersion halos presented by Cohen (2011) and Halley et al. (2015), which were derived from unprocessed univariate geochemical data. Copper and Mo addition define the primary magmatic hydrothermal fluid pathway that connects the metal-source region in the Luhr Hill cupola (Fig. 1; 5–6 km paleodepth) with the Ann Mason deposit at shallower depth (2.5 km paleodepth; Dilles, 1987; Dilles and Einaudi, 1992; Cohen, 2011). Copper depletion outside this primary fluid pathway (Fig. 6E) is consistent with previous mass balance work performed by Dilles and Einaudi (1992). This work showed that up to 30% of the Cu endowment in the Ann Mason deposit may have been leached from surrounding wall rocks, particularly the McLeod Hill monzodiorite.

Copper depletion observed in the McLeod Hill monzodiorite does not appear to be a function of abnormally high Cu values in least-altered samples. The geometric mean value of our least-altered McLeod Hill monzodiorite is 136 ppm (Appendix B; $n = 3$). This value is higher than the average crustal abundance of a typical andesite (~75 ppm; Taylor, 1964; Halley et al., 2015), but consistent with unaltered average values published by Dilles (1987; 120 ppm Cu).

Arsenic and Sb have been removed from the core of the Ann Mason deposit, and added above and to the sides of the deposit between 1 and 2 km paleodepth (Fig. 6G and H). This is consistent with the results reported by Cohen (2011) and Halley et al. (2015), which showed that As depletion occurred where silicate alteration minerals dominate (K-feldspar, quartz) in the potassic core of a porphyry system. Arsenic addition at Ann Mason is most coherent above and adjacent to the deposit. This may correspond to the limit of the pyrite halo, which is restricted to a domain that extends 1.5 km south of the deposit centre (Dilles and Einaudi, 1992).

The strong addition of Sb to sample YE16AA063 (1100%; post-mineralisation Shamrock monzonite) outside of the Casting Copper deposit suggests that post-ore-forming endoskarn development in the Shamrock batholith was associated with the mobility of some key indicator elements like Sb and As. However, Cu depletion in this sample indicates that the mobility of Cu during endoskarn formation in the Shamrock monzonite is decoupled from the mobility of some key indicator elements like Sb and As.

Phosphorus addition is restricted to the shallow parts of the Yerington batholith (< 4 km paleodepth) with only minor P depletion recorded in any samples from the Ann Mason fault block (Fig. 6D). Previous studies have identified hydrothermal apatite ($Ca_5(PO_4)_3(F,Cl,OH)$) as part of three hydrothermal mineral assemblages in the Yerington district: (1) magnetite–apatite–chalcopyrite veins (Dilles et al., 2000); (2) quartz–calcite–hematite–magnetite veins with actinolite, chlorite, talc and minor apatite associated with skarn development (Dilles et al., 2000); and (3) quartz–oligoclase–titanite–rutile–apatite ± epidote ± actinolite in the sodic-calcic assemblage (Carten, 1986; Battles, 1990; Battles and Barton, 1995). In the advanced argillic environment associated with some porphyry deposits, P can be hosted in aluminum–phosphate–sulfate minerals that are typically intergrown with alunite (Sillitoe, 2010). However, P addition in the Ann Mason fault block is not spatially coincident with areas where argillic alteration has previously been described (i.e. Blue Hill; Dilles and Einaudi, 1992; Dilles et al., 2000). We attribute the addition of P to sodic-calcic alteration and the associated development of hydrothermal apatite, given the absence of Cu-sulfide-bearing apatite veins and the absence of skarn assemblages in the shallow, central parts of the Yerington batholith in the Ann Mason fault block.

5.2. Sodic-calcic alteration vs. propylitic alteration

Previous workers have recorded sodic-calcic alteration in the deep (eastern) parts of the Yerington batholith, typically below 3.5 km paleodepth (Carten, 1986; Dilles and Einaudi, 1992; Dilles et al., 1992; Dilles et al., 1995; Dilles et al., 2000). Our mass balance results from the deeper parts of the Yerington batholith are generally consistent with Ca and Na addition associated with sodic-calcic alteration (Fig. 6A and C), a key feature of the alteration assemblage described by Carten (1986). Fig. 2M (sample YE16AA001) shows an example of typical sodic-calcic alteration described by Carten (1986) and Dilles and Einaudi (1992): clots of epidote (up to 20 cm diameter) with albite alteration halos. Addition and depletion results for sample YE16AA001 show that Ca has been strongly added (131%), and Na weakly added (41%). However, not all albite-altered samples from the deep parts of the Yerington batholith record Na addition. Sample YE16AA002, epidote–albite-altered Luhr Hill granite, shows strong Ca addition (140%) but Na is depleted (−31%). Furthermore, the majority of samples within or adjacent to the Luhr Hill cupola show negligible mass change of Na (−25

Table 4
Comparison of CaO and Na_2O values between geometric mean values for least-altered samples calculated in this study, and unaltered samples published by Dilles (1987).

	Calculated geometric mean values (This study)		Dilles (1987) unaltered samples	
	CaO (%)	Na_2O (%)	CaO (%)	Na_2O (%)
Luhr Hill granite	3.0	4.3	2.9	4.1
Bear monzonite	4.1	4.1	3.6	3.8
McLeod Hill monzodiorite	4.6	4.2	5.9	4.6

to 25%; Fig. 6C). These results suggest that (1) Na addition is not necessary to form albite-bearing alteration assemblages (i.e., sample YE16AA002); and (2) Na addition may not be required to form albite in the sodic-calcic alteration assemblage. Geometric mean values for Ca and Na in our least-altered samples are comparable to unaltered sample values presented by Dilles (1987; Table 4). This similarity precludes our least-altered sample selection from being the cause for the lack of consistent Na addition at depth in the Yerington batholith.

Strong Na addition associated with albite alteration in the deep parts of the Yerington batholith does occur outside the Ann Mason fault block. The Albite Hills area, named for its bleached appearance and high albite content of the rocks, is located approximately 10 km northeast of the Ann Mason deposit in a separate fault block (not shown in Fig. 1). Sample YE16AA011 records 134% Na addition and 78% Ca addition. Drill core samples YE16AA244 (Fig. 2N) and YE16AA245 from the same area record 98% and 106% Na addition, respectively.

Sodium addition is not restricted to the deep parts of the Yerington batholith (Fig. 6C) and occurs above the 4 km paleodepth mark in the shallower (western) parts of the batholith. This area corresponds to the propylitic alteration zone described by Carten (1986) and Dilles and Einaudi (1992). Sample YE16AA170 (Fig. 2O) shows 136% Na addition. In hand sample, this Na addition corresponds to thin epidote–-quartz veins (~0.5 cm wide) with wide albite vein halos (15 cm diameter; Fig. 2O). This style of vein and alteration are common in the shallow parts of the Yerington batholith.

Because our sampling focused on epidote alteration, albite alteration might be considered as underrepresented in the samples. However, inspection of hand specimens indicates epidote and albite occur together (Fig. 2I–Q). The result of this concurrence is that sodic alteration is likely represented adequately.

Propylitic alteration in the Yerington district is traditionally understood to occur mainly by isochemical reactions in which albite forms by the loss of Ca from plagioclase, rather than by the metasomatic addition of Na (Carten, 1986). Therefore, the addition of Na in the shallow (< 4 km) alteration environment suggests: (1) sodic-calcic alteration is not restricted to deep parts of the Yerington batholith, as has previously been recorded; (2) sodic-calcic alteration can form albite and epidote without significant addition of Na; (3) propylitic alteration is not strictly isochemical, at least at the sample scale, and can involve the addition and depletion of major and trace element components; and/or (4) sodic-calcic alteration and propylitic alteration are different expressions of the same fluid.

It is possible that sodic-calcic alteration affected rocks in the shallow environment; however, sodic-calcic fluids are proposed to have infiltrated the Yerington batholith along structural conduits, primarily along the upper contact of the Luhr Hill cupola and along the main Luhr Hill porphyry dyke swarm (Carten, 1986; Dilles and Einaudi, 1992; Dilles et al., 2000). In 2-D map view, there are no obvious structural conduits to focus sodic-calcic fluids into the shallow, deposit-distal environment. Dilles and Einaudi (1992) have previously suggested that propylitic alteration in the Ann Mason fault block may be the shallow, distal expression of sodic-calcic alteration. However, this argument contradicts the oxygen and Sr-isotope data of altered rocks in the district, which show different source fluids, magmatic vs. non-magmatic-dominated, for propylitic and sodic-calcic altered samples respectively (Dilles et al., 1995).

Invoking a genetic association between propylitic alteration and sodic-calcic alteration may not be necessary to explain why epidote alteration in the shallow environment is not isochemical. A number of recent studies on epidote-altered rocks in the porphyry environment have shown that propylitic alteration is not isochemical. Pacey et al. (2016) showed that Ca, Fe, and Co were added to propylitically-altered rocks from the Northparkes Cu−Au deposit, Australia. Additionally, in situ analysis of epidote and chlorite using laser ablation inductively coupled mass spectrometry demonstrates that, on the district scale, the major and trace element chemistry of these minerals changes significantly from the deposit centre to the distal alteration margins (Cooke et al., 2014b; Wilkinson et al., 2015; Wilkinson et al., 2017). These studies raise the issue of the scale of sampling.

Epidote-altered rocks in the Ann Mason fault block record significant addition and depletion of both major and trace elements (< −25 depletion; > 25% addition). These elements may have been derived locally from rocks immediately outside the area sampled for whole rock geochemical analysis (within 10 m; outcrop scale). The elements may have been scavenged from other rocks by deeply circulating fluids (within 5 km; camp scale). Conversely, elements may have been contributed directly from a magmatic-hydrothermal fluid, or from a non-magmatic hypersaline brine.

Samples from the Yerington and Shamrock batholiths record either P addition (> 25%) or no net change (−25 or 25%; Fig. 6D). There is no evidence of P scavenging in one part of the fault block that would account for the addition of P at shallow levels in the Yerington batholith. It is therefore likely that P was introduced to host rocks by an externally-sourced fluid (i.e. magmatic hydrothermal). Calcium, on the other hand, is depleted in samples from the deposit centre, and added to samples outside the deposit centre (Fig. 6A). This pattern suggests that Ca was not necessarily added to the system from an external source, just moved from one part of the fault block to another.

6. Conclusions

Element addition and depletion maps in the Ann Mason fault block, Yerington district, Nevada, illustrate quantitative chemical changes related to porphyry mineralisation and hydrothermal alteration. We account for the natural heterogeneity of protolith samples by calculating an envelope of uncertainty around mass balance isocons, and limit false mass balance results caused by background geochemical variance. Binned classes of mass change intensity further reduce the effects of rock heterogeneity on calculated results.

Copper and Mo addition in the core of the Ann Mason deposit is spatially associated with Ca and Sr depletion (approaching total loss, −100%) due to the destruction of Ca-plagioclase during potassic alteration. Calcium (up to 1570%) and Sr (up to 315%) addition patterns are coincident with epidote alteration and define a 4 km addition halo around Ann Mason, unrelated to protolith composition. Arsenic and Sb were removed from the deposit centre (approaching −100%) where silicate-mineral alteration assemblages dominate. Antimony was weakly added (< 1000%) outside the main magmatic hydrothermal fluid pathway. Samples from the post-mineralisation Shamrock batholith record strong Ca addition (up to 554%), and Na depletion (down to −98%) at the northern contact of the Shamrock batholith with host carbonate rocks is coincident with strong epidote alteration.

Samples from the deep parts of the Yerington batholith (> 4 km paleodepth) in the Ann Mason fault block commonly contain the alteration assemblage epidote–albite ± actinolite ± titanite (Fig. 2M and N). These samples are typically associated with the strong addition of Ca and the weak addition of Na, and correspond to the sodic-calcic alteration assemblage previously described in the district (Carten, 1986;

Dilles and Einaudi, 1992). In contrast to this previous work, we found that Na and Ca were also added to rocks in the shallow parts of the Yerington batholith (< 4 km). Addition of these elements at shallow depth may correspond to a shallow, distal expression of sodic-calcic alteration (Dilles and Einaudi, 1992) or to non-isochemical processes associated with propylitic alteration. Mass transfer in epidote-altered rocks is significant (> 25%) both proximal and distal to the Ann Mason porphyry deposit centre. Our results support the interpretation of propylitic alteration as representing extensive chemical mobility, rather than local isochemical reactions, and the use of epidote-altered rocks to understand mineralising systems at district-scale.

Supplementary data to this article can be found online at https://doi.org/10.1016/j.gexplo.2018.09.009.

Acknowledgements

This research is part of a broader PhD project funded by the AMIRA International P1153 project 'Applying the explorer's toolbox to discover Cu, Au, and Mo deposits', an Australian Postgraduate Award, and an AusIMM Education Endowment Fund scholarship. Samples were collected in 2016 and 2017 with invaluable assistance from Angela Escolme, Josh Phillips, Amos Garay, Mike Baker and Lejun Zhang. We wish to sincerely thank the detailed comments and suggestions received during manuscript review from Jeremy Richards and an anonymous reviewer, they greatly improved the paper. Appreciation is also given to John Dilles and Dick Tosdal for geological discussions and descriptions of key field relationships during the 2016 'Field Mapping of Ore-deposits Course' held at Yerington. Further thanks to Matt Cunningham and Tom Watkins of Mason Resources, George Eliopolous and Todd Bonsall from Quaterra Resources, and Rana Gill and Hank Ohlin from Mason Valley Copper for property access, drill core access, and geological discussions in the field. Early framing for this manuscript benefited from unpublished mass balance work done by Rob Scott and David Doutch at the University of Tasmania.

References

Aitchison, J., 1989. Reply to "interpreting and testing compositional data" by Alex Woronow, Karen M. Love, and John C. Butler. Math. Geol. 21, 65–71.
Allegre, C.J., Lewin, E., 1995. Scaling laws and geochemical distributions. Earth Planet. Sci. Lett. 132, 1–13.
Armbruster, T., Bonazzi, P., Akasaka, M., Bermanec, V., Chopin, C., Gieré, R., Heuss-Assbichler, S., Liebscher, A., Menchetti, S., Yuanming, P., 2006. Recommended nomenclature of epidote-group minerals. Eur. J. Mineral. 18, 551–567.
Battles, D., 1990. The Hydrothermal Evolution of the Shamrock Batholith, Western Nevada, and the Origin of Sodium-rich Alteration in the Western United States (PhD thesis). University of California (122p).
Battles, D.A., Barton, M.D., 1995. Arc-related sodic hydrothermal alteration in the western United States. Geology 23, 913–916.
Brand, N.W., 1999. Element ratios in nickel sulphide exploration:vectoring towards ore environments. . Geochem Expl. 67, 145–165.
Brauhart, C.W., Grunsky, E.C., Hagemann, S.G., 2017. Magmato-hydrothermal space: a new metric for geochemical characterisation of metallic ore deposits. Ore Geol. Rev. 86, 867–895.
Carranza, E.J.M., 2017. Geochemical Mineral Exploration: should we use enrichment factors or log-ratios? Nat. Resour. Res. 26, 411–428.
Carten, R.B., 1986. Sodium-calcium metasomatism; chemical, temporal, and spatial relationships at the Yerington, Nevada, porphyry copper deposit. Econ. Geol. 81, 1495–1519.
Chandrajith, R., Dissanayake, C., Tobschall, H., 2001. Application of multi-element relationships in stream sediments to mineral exploration: a case study of Walawe Ganga Basin, Sri Lanka. Appl. Geochem. 16, 339–350.
Chen, Z., Chen, J., Tian, S., Xu, B., 2017. Application of fractal content-gradient method for delineating geochemical anomalies associated with copper occurrences in the Yangla ore field, China. Geosci. Front. 8, 189–197.
Coelho, J., 2006. GEOISO—a Windows™ program to calculate and plot mass balances and volume changes occurring in a wide variety of geologic processes. Comput. Geosci. 32, 1523–1528.
Cohen, J., 2011. Mineralogy and Geochemistry of Hydrothermal Alteration at the Ann-Mason Porphyry Copper Deposit, Nevada: Comparison of Large-scale ore Exploration Techniques to Mineral Chemistry (MSc thesis). Oregon State University (111 p).
Cooke, D.R., Bull, S.W., Donovan, S., Rogers, J.R., 1998. K-metasomatism and base metal depletion in volcanic rocks from the McArthur Basin, Northern Territory; implications for base metal mineralization. Econ. Geol. 93, 1237–1263.
Cooke, D.R., Baker, M., Hollings, P., Sweet, G., Chang, Z., Danyushevsky, L., Gilbert, S., Zhou, T., White, N.C., Gemmell, J.B., 2014a. New advances in detecting the distal geochemical footprints of porphyry systems—Epidote mineral chemistry as a tool for vectoring and fertility assessments. Econ. Geol. 18, 127–152.
Cooke, D.R., Hollings, P., Wilkinson, J.J., Tosdal, R.M., 2014b. Geochemistry of porphyry deposits. In: Holland, H.D., Turekian, K.K. (Eds.), Treatise on Geochemistry, Second edition. vol. 13. pp. 357–381.
Dilles, J.H., 1984. The petrology and geochemistry of the Yerington batholith and the Ann-Mason porphyry copper deposit, Western Nevada. Stanford University, California, pp. 522.
Dilles, J.H., 1987. Petrology of the Yerington Batholith, Nevada; evidence for evolution of porphyry copper ore fluids. Econ. Geol. 82, 1750–1789.
Dilles, J.H., Einaudi, M.T., 1992. Wall-rock alteration and hydrothermal flow paths about the Ann-Mason porphyry copper deposit, Nevada; a 6-km vertical reconstruction. Econ. Geol. 87, 1963–2001.
Dilles, J.H., Proffett, J., 1995. Metallogenesis of the Yerington batholith, Nevada: Porphyry copper deposits of the American Cordillera, Arizona. Geol. Soc. Digest. 20, 306–315.
Dilles, J.H., Wright, J.E., 1988. The chronology of early Mesozoic arc magmatism in the Yerington district of western Nevada and its regional implications. Geol. Soc. Am. Bull. 100, 644–652.
Dilles, J.H., Solomon, G.C., Taylor, H.P., Einaudi, M.T., 1992. Oxygen and hydrogen isotope characteristics of hydrothermal alteration at the Ann-Mason porphyry copper deposit, Yerington, Nevada. Econ. Geol. 87, 44–63.
Dilles, J.H., Farmer, G.L., Field, C.W., 1995. Sodium-calcium alteration by non-magmatic saline fluids in porphyry copper deposits: results from Yerington, Nevada. In: Mineralogical Association of Canada Short Course Series 23. pp. 309–338.
Dilles, J.H., Einaudi, M., Proffett, J., Barton, M., 2000. Overview of the Yerington porphyry copper district: magmatic to nonmagmatic sources of hydrothermal fluids: their flow paths and alteration effects on rocks and Cu-Mo-Fe-Au ores. In: Society of Economic Geologists Guidebook Series, vol. 32. pp. 55–66.
Dilles, J.H., Kent, A.J., Wooden, J.L., Tosdal, R.M., Koleszar, A., Lee, R., Farmer, L.P., 2015. Zircon compositional evidence for sulfur-degassing from ore-forming arc magmas. Econ. Geol. 110, 241–251.
Einaudi, M.T., 1977. Petrogenesis of the copper-bearing skarn at the Mason Valley Mine, Yerington District, Nevada. Econ. Geol. 72, 769–795.
El-Makky, A.M., Sediek, K.N., 2012. Stream sediments geochemical exploration in the northwestern part of Wadi Allaqi Area, South Eastern Desert, Egypt. Nat. Resour. Res. 21, 95–115.
Floyd, P., Winchester, J., 1978. Identification and discrimination of altered and metamorphosed volcanic rocks using immobile elements. Chem. Geol. 21, 291–306.
Ford, J., 1978. A chemical study of alteration at the Panguna porphyry copper deposit, Bougainville, Papua New Guinea. Econ. Geol. 73, 703–720.
Gazley, M., Collins, K., Roberston, J., Hines, B., Fisher, L., McFarlane, A., 2015. Application of principal component analysis and cluster analysis to mineral exploration and mine geology. In: AusIMM New Zealand Branch Annual Conference proceedings, Dunedin, New Zealand, pp. 131–139.
Gong, Q., Deng, J., Wang, C., Wang, Z., Zhou, L., 2013. Element behaviors due to rock weathering and its implication to geochemical anomaly recognition: a case study on Linglong biotite granite in Jiaodong peninsula, China. J. Geochem. Explor. 128, 14–24.
Govett, G.J.S., 1983. Handbook of Exploration Geochemistry. Elsevier (461 p).
Grant, J.A., 1986. The isocon diagram; a simple solution to Gresens' equation for metasomatic alteration. Econ. Geol. 81, 1976–1982.
Grant, J.A., 2005. Isocon analysis: a brief review of the method and applications. Phys. Chem. Earth 30, 997–1004.
Gresens, R.L., 1967. Composition-volume relationships of metasomatism. Chem. Geol. 2, 47–65.
Gustafson, L.B., Hunt, J.P., 1975. The porphyry copper deposit at El Salvador, Chile. Econ. Geol. 70, 857–912.
Halley, S., Dilles, J.H., Tosdal, R., 2015. Footprints: hydrothermal alteration and geochemical dispersion around porphyry copper deposits. In: Society of Economic Geologists Newsletter. 100. pp. 12–17.
Harris, N.B., Einaudi, M.T., 1982. Skarn deposits in the Yerington District, Nevada; metasomatic skarn evolution near Ludwig. Econ. Geol. 77, 877–898.
Hosseini-Dinani, H., Aftabi, A., Esmaeili, A., Rabbani, M., 2015. Composite soil-geochemical halos delineating carbonate-hosted zinc-lead-barium mineralization in the Irankuh district, Isfahan, west-central Iran. J. Geochem. Explor. 156, 114–130.
Huston, D.L., 1993. The effect of alteration and metamorphism on wall rocks to the Balcooma and Dry River South volcanic-hosted massive sulfide deposits, Queensland, Australia. J. Geochem. Explor. 48, 277–307.
Knopf, A., 1918. Geology and Ore Deposits of the Yerington District. US Government Printing Office, Nevada (68p).
Kulla, G., Oshust, P., Desautels, J.R.P., Melnyk, J., Zurowski, G., Jones, L., Colantonio, M., 2017. 2017 Updated Preliminary Economic Assessment on the Ann Mason Project Nevada. AMEC Foster Wheeler Americas Ltd., U.S.A (367p).
Large, R.R., Gemmell, J.B., Paulick, H., Huston, D.L., 2001. The alteration box plot: a simple approach to understanding the relationship between alteration mineralogy and lithogeochemistry associated with volcanic-hosted massive sulfide deposits. Econ. Geol. 96, 957–971.
Lipske, J.L., 2002. Advanced argillic and sericitic alteration in the Buckskin Range, Nevada; a product of ascending magmatic fluids from the deeper Yerrington porphyry copper environment. In: Geological Society of America Abstracts with Programs. Vol. 2002. pp. 15–16.
Liu, C., Hu, S., Ma, S., Tang, L., 2014. Primary geochemical patterns of Donggua Mountain laminar skarn copper deposit in Anhui, China. J. Geochem. Explor. 139,

152–159.
Lopez-Moro, F.J., 2012. EASYGRESGRANT-A Microsoft Excel spreadsheet to quantify volume changes and to perform mass-balance modeling in metasomatic systems. Comput. Geosci. 39, 191–196.
Lowell, J.D., Guilbert, J.M., 1970. Lateral and vertical alteration-mineralization zoning in porphyry ore deposits. Econ. Geol. 65, 373–408.
MacLean, W., Barrett, T., 1993. Lithogeochemical techniques using immobile elements. J. Geochem. Explor. 48, 109–133.
Martín-Fernández, J.A., Hron, K., Templ, M., Filzmoser, P., Palarea-Albaladejo, J., 2012. Model-based replacement of rounded zeros in compositional data: classical and robust approaches. Comput. Stat. Data Anal. 56, 2688–2704.
McKinley, J.M., Hron, K., Grunsky, E.C., Reimann, C., de Caritat, P., Filzmoser, P., van den Boogaart, K.G., Tolosana-Delgado, R., 2016. The single component geochemical map: fact or fiction? J. Geochem. Explor. 162, 16–28.
Monecke, T., Monecke, J., Herzig, P.M., Gemmell, J.B., Mönch, W., 2005. Truncated fractal frequency distribution of element abundance data: a dynamic model for the metasomatic enrichment of base and precious metals. Earth Planet. Sci. Lett. 232, 363–378.
Olade, M., Fletcher, W., 1976. Trace element geochemistry of the Highland Valley and Guichon Creek Batholith in relation to porphyry copper mineralization. Econ. Geol. 71, 733–748.
Pacey, A., Wilkinson, J.J., Boyce, A.J., Cooke, D.R., 2016. Propylitic alteration and metal mobility in porphyry systems: a case study of the Northparkes Cu-Au deposits, NSW, Australia. Appl. Earth Sci. 125, 93.
Proffett Jr., J.M., 1977. Cenozoic geology of the Yerington district, Nevada, and implications for the nature and origin of Basin and Range faulting. Geol. Soc. Am. Bull. 88, 247–266.
Proffett, Jr., J.M., and Dilles, J.H., 1984, Geologic map of the Yerington district, Nevada: Nevada Bureau of Mines and Geology Map 77, scale 1:24,000, 1 sheet.
Reimann, C., 2005. Geochemical mapping: technique or art? Geochem. Explor. Environ. Anal. 5, 359–370.
Reimann, C., Filzmoser, P., 2000. Normal and lognormal data distribution in geochemistry: death of a myth. Consequences for the statistical treatment of geochemical and environmental data. Environ. Geol. 39, 1001–1014.
Richardson, C.A., Seedorff, E., 2015. Reconstruction of normal fault blocks in the Ann-Mason and Blue Hill areas, Yerington district, Lyon County, Western Nevada. In: Pennell, W.M., Garside, L.J. (Eds.), New concepts and discoveries: Proceedings, Geological Society of Nevada Symposium. 2. pp. 1153–1178.
Riverin, G., Hodgson, C., 1980. Wall-rock alteration at the Millenbach Cu-Zn mine, Noranda, Quebec. Econ. Geol. 75, 424–444.
Rolland, Y., Cox, S., Boullier, A.M., Pennacchioni, G., Mancktelow, N., 2003. Rare earth and trace element mobility in mid-crustal shear zones: Insights from the Mont Blanc Massif (Western Alps). Earth Planet. Sci. Lett. 214, 203–219.
Rollinson, H.R., 1993. Using Geochemical Data: Evaluation, Presentation, Interpretation. Routledge, Longman, Harlow (352p).
Schöpa, A., Annen, C., Dilles, J.H., Sparks, R.S.J., Blundy, J.D., 2017. Magma emplacement rates and porphyry copper deposits: thermal modeling of the Yerington Batholith, Nevada. Econ. Geol. 112, 1653–1672.
Seedorff, E., Dilles, J.H., Proffett Jr., J.M., Einaudi, M., Zurcher, L., Stavast, W., Johnson, D., Barton, M., 2005. Porphyry deposits: Characteristics and origin of hypogene + features. In: Economic Geology 100th Anniversary Volume. 29. pp. 251–298.
Sillitoe, R.H., 2010. Porphyry copper systems. Econ. Geol. 105, 3–41.
Sturm, R., 2003. SHEARCALC—A computer program for the calculation of volume change and mass transfer in a ductile shear zone. Comput. Geosci. 29, 961–969.
Taylor, S., 1964. Abundance of chemical elements in the continental crust: a new table. Geochim. Cosmochim. Acta 28, 1273–1285.
Ulrich, T., Heinrich, C.A., 2002. Geology and alteration geochemistry of the porphyry Cu-Au deposit at Bajo de la Alumbrera, Argentina. Econ. Geol. 97, 1865–1888.
Villaplaza, B.R.B., Buena, A.E., Pacle, N.A.D., Payot, B.D., Gabo-Ratio, J.A.S., Ramos, N.T., Dimalanta, C.B., Faustino-Eslava, D.V., Queaño, K.L., Yumul Jr., G.P., 2017. Alteration and lithogeochemistry in the Masara gold district, Eastern Mindanao, Philippines, as tools for exploration targeting. Ore Geol. Rev. 91, 530–540.
Vistelius, A.B., 1960. The skew frequency distributions and the fundamental law of the geochemical processes. J. Geol. 68, 1–22.
Wang, C., Carranza, E.J.M., Zhang, S., Zhang, J., Liu, X., Zhang, D., Sun, X., Duan, C., 2013. Characterization of primary geochemical haloes for gold exploration at the Huanxiangwa gold deposit, China. J. Geochem. Explor. 124, 40–58.
Waters, D.J., 2001. The significance of prograde and retrograde quartz-bearing intergrowth microstructures in partially melted granulite-facies rocks. Lithos 56, 97–110.
Watkins, T., Page, N., Gant, J., Cunningham, M., Hartman, B., 2015. Ann-Mason porphyry copper deposit Yerington district, Lyon Country, NV. In: Geological Society of Nevada Symposium, Reno, Nevada, USA, 2015, Conference Presentation, (40p).
White, A.J., 2017. AutoIsocon, v.1. In: CSIRO Software Collection, https://doi.org/10.4225/08/595302320f5ae.
White, A.J., Pearce, M.A., Meadows, H.R., 2016. Distinguishing regional-and local-scale metasomatic systems at the Prairie Downs Zn-Pb deposit. Lithos 262, 247–265.
Wilkinson, J.J., Chang, Z., Cooke, D.R., Baker, M.J., Wilkinson, C.C., Inglis, S., Chen, H., Gemmell, J.B., 2015. The chlorite proximitor: a new tool for detecting porphyry ore deposits. J. Geochem. Explor. 152, 10–26.
Wilkinson, J.J., Baker, M., Cooke, D.R., Wilkinson, C.C., Inglis, S., 2017. Exploration targeting in porphyry Cu systems using propylitic mineral chemistry: a case study of the El Teniente deposit, Chile. In: Conference Paper, 14th SGA Biennial Meeting, Quebec, Canada. 2017 (4p).
Winchester, J.A., Floyd, P.A., 1977. Geochemical discrimination of different magma series and their differentiation products using immobile elements. Chem. Geol. 20, 325–343.
Yaylalı-Abanuz, G., 2013. Determination of anomalies associated with Sb mineralization in soil geochemistry: a case study in Turhal (northern Turkey). J. Geochem. Explor. 132, 63–74.
Zuo, R., Xia, Q., Wang, H., 2013. Compositional data analysis in the study of integrated geochemical anomalies associated with mineralization. Appl. Geochem. 28, 202–211.
Zuo, R., Carranza, E.J.M., Wang, J., 2016. Spatial analysis and visualisation of exploration geochemical data. Earth Sci. Rev. 158, 9–18.